Article

Examining the Impact of Coal Contamination on Soil Structural and Moisture Properties: A Comparative Study of Coal-Free and Coal-Impacted Soils

Wenjing Zhang [1,2], Xiaoju Nie [3,*], Tongqian Zhao [1,*] and Xuan Liu [3]

1 School of Resources and Environment, Henan Polytechnic University, Jiaozuo 454003, China; zhangwenjing9899@163.com
2 School of Surveying and Land Information Engineering, Henan College of Surveying and Mapping, Zhengzhou 451464, China
3 School of Surveying and Land Information Engineering, Henan Polytechnic University, Jiaozuo 454003, China; keystonelx@hpu.edu.cn
* Correspondence: niexj2005@hpu.edu.cn (X.N.); zhaotq@hpu.edu.cn (T.Z.)

Abstract: Soil porosity and moisture are critical indicators of soil quality. In coal–grain intercropping areas, centuries of coal industry activities have resulted in coal particle contamination, which has affected soil properties; however, its impact on soil porosity and moisture remains underexplored. This study compares coal-contaminated soils (CCS) and coal-free soils (CFS) in Jiaozuo, employing computed tomography (CT) scanning and moisture measurements to analyze how coal pollution influences soil porosity and moisture. Our findings indicate that CCS, compared to CFS, exhibit significant reductions in total porosity (TP), CT-measured porosity (CTP), number of pores (CTN), and the proportion and volume of water–air regulating pores (CTNWA/CTN and CTPWA). These results underscore that coal pollution substantially alters soil porosity and pore numbers. Additionally, coal pollution modifies soil pore morphology, leading to reductions in the number and length of pore throats (N_{throat} and L_{throat}) and causing the pores to become more flattened and rounded, with an increased inclination angle of interconnected pores (IA_{ic}). As coal pollution levels increase, interconnected porosity (P_{ic}) and coordination number (CN_{ic}) decrease, while isolated porosity ($P_{isolated}$) increases. In terms of moisture parameters, coal pollution diminishes the maximum water holding capacity, soil permanent wilting point, saturated hydraulic conductivity, and moisture evaporation rate. In contrast, field water-holding capacity and maximum effective water content are enhanced. Furthermore, with increased coal pollution, maximum water holding capacity, soil permanent wilting point, and saturated hydraulic conductivity decreased, whereas field water-holding capacity and maximum effective water content increased. Correlation analysis reveals that changes in CTN, N_{throat}, and L_{throat} significantly influence moisture parameter variations, with most pore parameter changes affecting saturated hydraulic conductivity. The observed effects of coal pollution on soil pore parameters are attributed to the filling and clogging actions of coal particles, while its impact on moisture parameters primarily results from these particles filling and clogging soil pores. This study provides a scientific basis for managing soil moisture in areas affected by coal pollution, particularly in coal–grain intercropping regions.

Keywords: coal-contaminated soil; pore characteristics; soil moisture properties; X-ray computed tomography; coal–grain intercropping area

1. Introduction

Since the mid-18th century, the extensive use of coal has led to the significant deposition of coal particles in terrestrial soils, particularly in China's coal–grain intercropping regions. These areas, which account for 42.7% of the nation's arable land, are crucial for preserving arable land and ensuring food security [1]. Despite their importance, the issue of

coal-polluted soil in these regions remains underexplored. Studies have demonstrated that coal-derived carbon, a form of geogenic carbon distinct from true plant-derived organic carbon, can lead to an overestimation of the soil organic matter content, accelerating the mineralization and decomposition of soil organic matter [2]. Soil fertility and crop growth are heavily reliant on soil water and gas properties, which are reflected by soil porosity and moisture. These key indicators are influenced by coal particles, an exogenous pollutant, highlighting the need for a deeper understanding of their effects on soil pore structure and moisture characteristics.

The influence of exogenous pollutants from coal mining, such as coal gangue, fly ash, and coal slime, on soil has been a primary focus of research. For instance, fly ash alters soil properties, pH, and moisture characteristics due to its large surface area and significant porosity [3,4]. The addition of fly ash has been shown to enhance pore development in the 6–45 μm range in clay [5] and improve soil water retention, benefiting arid regions and mine reclamation efforts [6,7]. In contrast, coal gangue, with its coarser texture, higher porosity, and larger pore size, facilitates faster water movement [8]. The interlayer pore differences in reclaimed soil with coal gangue are significantly greater than those in typical layered soils, affecting the movement of water, nutrients, and air in the surface soil [9]. Additionally, coal gangue has well-developed macropores, allowing gases to preferentially pass through these larger pores [10]. This indicates that the porosity of external materials is a key factor affecting soil structure. However, fly ash, transformed by high-temperature combustion, cannot fully represent the soil changes in coal mining areas. Conversely, coal slime, a byproduct of coal production, has been found to improve overburden soil in mining areas by reducing density and increasing water holding capacity [11]. Its role in coal dust dispersion and mine water irrigation-derived coal particle contamination of soil warrants further attention, as a lack of information regarding such impacts limits our understanding of land management in the mining areas.

The microstructure of soil, particularly its porosity, plays a pivotal role in determining the soil's physical, hydraulic, and mechanical properties [12–15]. Researchers have employed various methods to analyze soil pore structures, including a visual inspection [16], resistivity measurement [17], scanning electron microscopy (SEM) [18], and mercury intrusion porosimetry (MIP) [19]. However, traditional techniques like MIP and SEM face challenges in effectively characterizing and quantifying changes in soil microstructure [20]. In contrast, X-ray computed tomography (CT) has gained prominence for its non-destructive approach, precise quantification, and three-dimensional (3D) visualization capabilities in studying soil pore structures [21]. Although CT experiments have initially been used to examine the internal soil structures and changes in the soil pore patterns during water infiltration [15], research on pore structure variations in coal-polluted soils within coal–grain intercropping areas remains limited.

Building upon soil X-ray micro-CT research, studies have extensively investigated soil pore characteristics under various conditions and influencing factors, including plant roots [22], soil fauna [23], and environmental processes like wet–dry and freeze–thaw cycles [21,24], alongside human interventions like the addition of amendments and mechanical compaction [20,25]. Research highlights the importance of the spatial geometric shape of pores in influencing soil moisture properties, with factors such as porosity, pore number, length, and coordination number being critical for water flow and solute transport. Soil permeability, a key moisture characteristic, has been examined through seepage simulations. Ferreira et al. [26] compared three CT-based methods for estimating soil aggregate pore spaces, providing alternatives for large image dataset processing. Min et al. [27] utilized 3D CT scans to study large pore characteristics in different fill substrates, simulating soil infiltration and assessing fill substrate impacts on soil functions through seepage simulations. Ran et al. [28] explored the porosity and connectivity of granite residual soil affected by wet–dry cycles, noting significant increases in permeability and hydraulic conductivity.

Despite these advancements, comprehensive studies integrating micro-CT results with actual moisture data to fully understand soil's 3D pore structure and moisture charac-

teristics are scarce, particularly regarding the impact of coal pollution from the mining areas on soil pore structure and hydraulic properties. Thus, this study focuses on the Jiaozuo coal–grain intercropping area, characterized by extensive coal-polluted soil. By employing CT scanning and soil moisture measurement techniques, it compares the soil pore structures and moisture characteristics of coal-contaminated soils (CCS) and coal-free soils (CFS). The goal is to elucidate the interconnected mechanisms by which coal pollution alters soil pores and moisture characteristics, offering valuable insights into the dynamics of soil properties under the influence of coal pollution.

2. Materials and Methods

2.1. Study Area

The research area, situated in the Jiaozuo mining region (35°18′ N, 113°17′ E), represents a typical coal–grain intercropping zone (Figure 1). This region experiences a warm temperate continental monsoon climate, characterized by an average annual temperature of 14.0 °C and an average annual rainfall of about 589.1 mm, with around 80% of precipitation occurring between July and August. The area's annual average evaporation rate varies between 1680 and 2041 mm. The prevailing wind direction is northeast and southwest, northerly in winter and southerly in summer. The topography predominantly consists of plains, mainly used for agricultural purposes. The soil, primarily limy brown earth with a loamy texture (sand/silt/clay ratio of 23%:67%:7%), has a pH of 8.14–8.48 [29]. Jiaozuo's mining history spans over 120 years, earning it recognition as a "century-old coal city". Prolonged mining activities have led to significant coal pollution in the area, and measurements have shown that heavy metal levels in the soil do not exceed national standards.
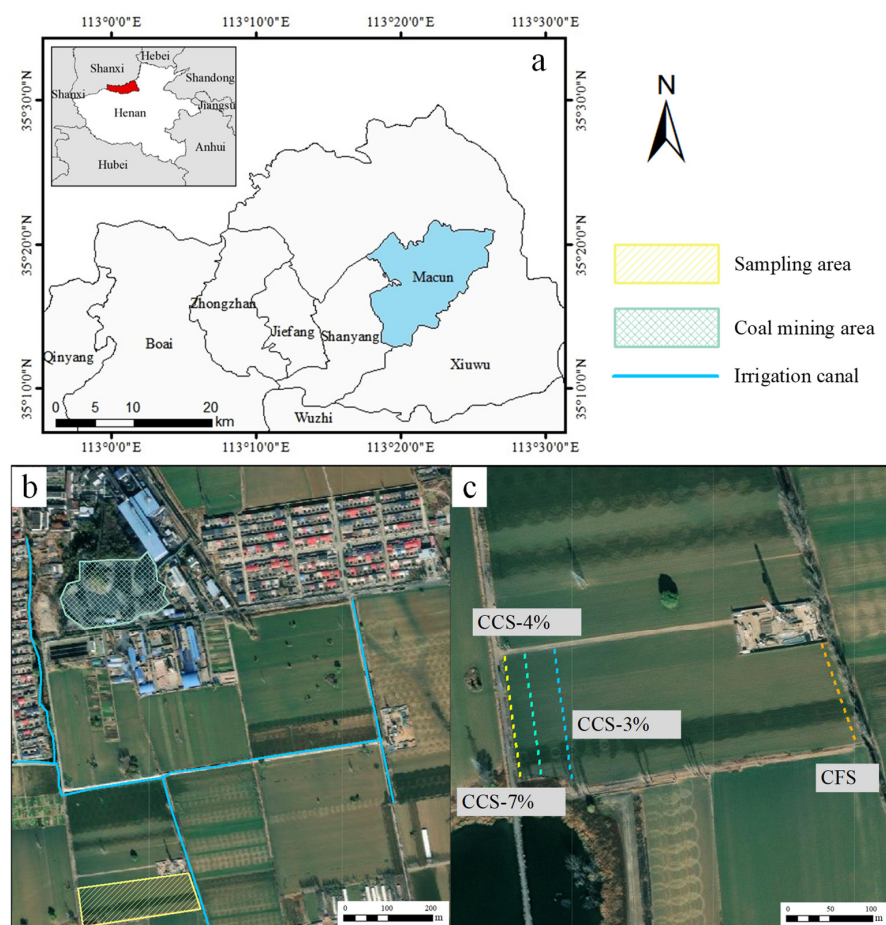
Figure 1. Study area. (**a**) Map of Macun District, Jiaozuo City, Henan Province, China. (**b**) Distribution map of coal mining sites and irrigation canals in and around the sampling area. (**c**) Schematic diagram showing the specific locations of CFS, CCS-3%, CCS-4%, and CCS-7% samples.

There are two predominant forms of coal pollution in the soil. The first results from coal dust dispersion, primarily occurring within a 20 m radius of coal transport routes. This type of pollution is relatively light, affecting the soil to a depth of less than 20 cm. The second form arises from long-term irrigation with mine water laden with suspended coal particles, a practice ongoing for over 60 years. This has led to more severe soil pollution, reaching depths of about 30 cm and extending up to 40 cm in some areas. Such pollution is commonly observed in agricultural zones within the mining area. The intensity of coal pollution in the soil gradually diminishes from the field's head to tail, as suspended coal particles in the mine water settle under the influence of gravity. The maximum extension of pollution is approximately 60 m. Beyond this point, the soil remains unpolluted due to the clarification of the mine water. Scanning electron microscope (SEM, Merlin Compact, Zeiss, Hamburg, Germany) examinations have revealed that coal particles in CCS are typically smaller than 0.25 mm in diameter, predominantly ranging between 7.02 to 107.5 μm (as shown in Figure 2). This means they are equivalent to the fine sand and silt particle size fractions in soil. These particles, with more than 80% being smaller than 0.075 mm, exhibit poor porosity. Their specific surface area and micropore volume are significantly lower at 2.08 m^2/g and 0 m^2/g, respectively, in comparison to soil particles which measure 11.66 m^2/g and 6.8×10^{-3} m^2/g.
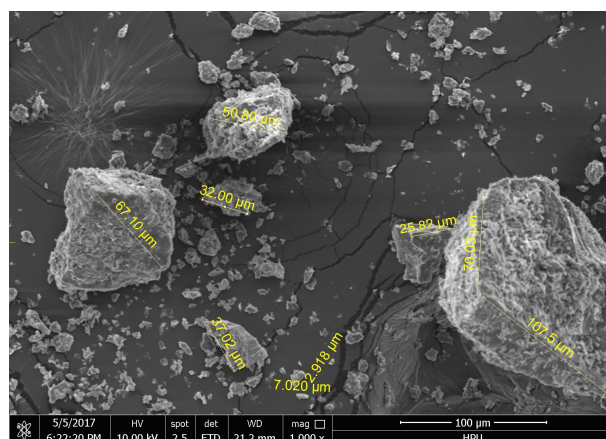
Figure 2. SEM image of coal slime particles.

2.2. Soil Sampling Collection

Sampling in the Jiaozuo agricultural field was carried out in April 2023, coinciding with the jointing stage of wheat, six months following the harvest and tillage of the preceding corn season. This timing ensured the soil was naturally settled and stable. For this study, a 260 m long and 3 m wide agricultural field, subjected to consistent farming practices and affected by coal pollution, was selected. Within a 40 m section of this field, CCS samples were systematically collected at distances of 1 m, 20 m, and 35 m from the field's edge. By identifying the different δ^{13}C or δ^{14}C signals of coal-derived carbon (C3) and plant-derived carbon (C4 or C3-C4 composite) [30–32], the levels of coal pollution at these three locations were quantified. The results showed that the coal-derived carbon content (the amount of coal-derived carbon per unit mass of dried soil) was 7% (7%-CCS, 1 m from the field's edge), 4% (4%-CCS, 20 m from the field's edge), and 3% (3%-CCS, 35 m from the field's edge). In contrast, CFS samples with 0% coal-derived carbon were obtained from an unpolluted zone 250 m from the edge. To ensure replicability, three sampling points were designated at each location, spaced 1 m apart.

Based on previous carbon isotope tracing research, coal pollution in the farmland of the study area is mainly concentrated within the 0–20 cm depth range [33]. Considering that the top 5 cm of soil is easily disturbed, the first step in the soil sampling procedure involved removing the top 5 cm of surface soil. Then, at each sampling point, six undisturbed soil samples were extracted from the 5–10 cm depth using a steel ring cutter (5 cm

height × 5 cm diameter). Of these, five samples were allocated for assessing the maximum water holding capacity, field water holding capacity, capillary water holding capacity, moisture evaporation rate dynamics, and soil bulk density. The sixth sample was air-dried in the laboratory for soil permanent wilting point. Additionally, one CT sample per sampling point was taken using a PVC ring cutter of identical dimensions, immediately wrapped in cling film for soil pore characteristic analysis. For the soil saturated hydraulic conductivity, undisturbed samples were collected using a steel ring cutter (5 cm high × 8 cm inner diameter). In total, the study involved the collection of 96 undisturbed soil samples, all transported to the laboratory for subsequent testing.

2.3. Sample Determination

2.3.1. Soil Pore Parameters

Total porosity (TP) was calculated from the product of soil bulk density and maximum water holding capacity. Additional porosity parameters were assessed using CT scanning, a technique leveraging X-rays for sectional structure imaging, known for its rapid data acquisition, non-destructive sampling approach, and visualized results [34]. This method offers detailed insights into the sample's material composition, internal structure, and potential defects within a specific scale [35].

The study employed the Phoenix V | tome | x S240 industrial CT scanning system (Huerth, Germany) for scanning. Each sample was securely fixed at the bottom of a glass column and then placed in the scanner. Scanning parameters included a voltage of 150 kV, a current of 130 μA, a resolution of 14 μm, an exposure time of 1000 ms, 1500 projections, and a total scanning time of 59 min. Consistent conditions were maintained for all 12 scans. Post-scanning, CT data were reconstructed using Phoenix Datos | x 2.0 software to produce clear 3D grayscale images. For image extraction and analysis, ImageJ 1.x and Avizo2019.1 software were utilized, adhering to the following workflow:
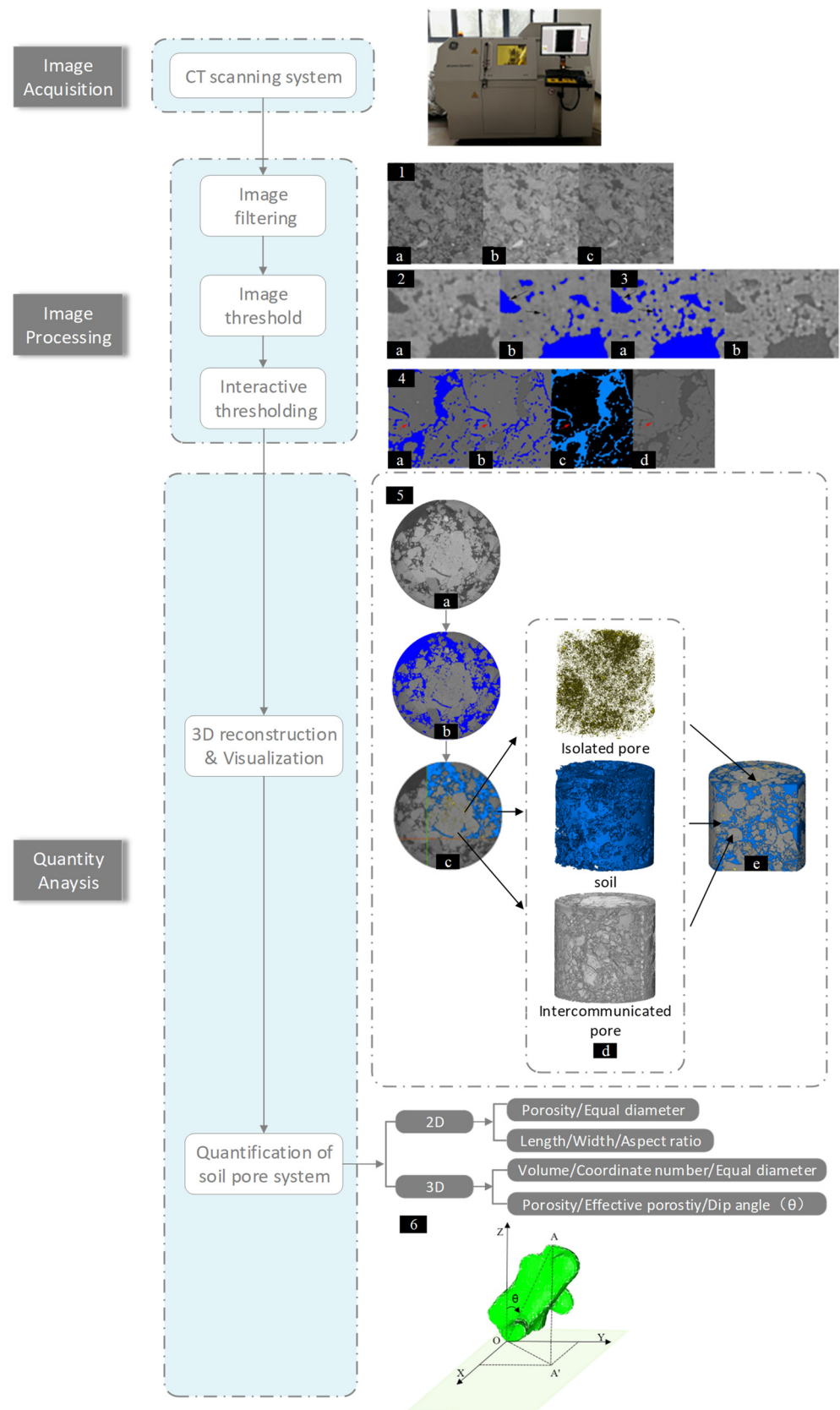
- Image calibration

CT scan images often contain noise resulting from the detector noise and external environmental interference. To minimize noise impacts on image processing, denoising filters were applied. Avizo offers several filtering options including linear filtering, median filtering, and non-local means filtering. Linear filtering is disregarded due to its non-adaptability, which compromises edge and detail preservation. Although median filtering [36] can circumvent this issue by selecting the median grayscale value in a specific region, it overlooks structural information. Hence, non-local means filtering was chosen for this study.

As illustrated in Figure 3(1), the noise reduction is evident. However, due to partial volume effects, the gray transition zones emerge at the junctions between the solid phase and pores of the soil. To mitigate this effect and enhance image segmentation accuracy, an unsharp mask module was utilized for edge enhancement. A comparison of Figure 3(2b,3b) clearly shows that following the edge enhancement, finer pores are more accurately identifiable during threshold segmentation, as indicated by the arrows.

- Threshold segmentation and three-dimensional reconstruction

The construction of an accurate soil pore model hinges on effective threshold segmentation. This crucial step transitions the process from image processing to image analysis, with the aim of distinguishing the soil's solid phase from its pores. After analyzing the corrected images, numerous small pores and cracks become evident. For segmenting larger pore regions, interactive thresholding was utilized, while Top-hat segmentation was applied for localizing and segmenting small pores and cracks, as depicted in Figure 3(4a,4b). By combining images processed through both methods, a comprehensive and accurately segmented image was obtained. Comparing the original image (Figure 3(4d)) with the segmented version (Figure 3(4c)) highlights the predominant selection of target areas. A 3D reconstruction of the binarized images post-threshold segmentation provides a clearer visualization of the spatial distribution and structure of soil pores (Figure 3(5)).

Figure 3. The flowchart for CT image calibration and data processing analysis (The calibration process of the CT images is detailed through Steps (**1**) to (**4**), leading to the reconstruction of three-dimensional soil models, as outlined in Step (**5**). Specifically, (**1a**) is the original slice image, (**1b**) is an image that has been denoised with non-local mean, (**1c**) is the image after adjusting the contrast. (**2a**) is the grayscale

image before edge enhancement using the Unsharp Mask, (**2b**) The segmented image before edge enhancement using an unsharp mask. (**3a**) Segmented image after edge enhancement using unsharp mask, (**3b**) is the grayscale image after edge enhancement using unsharp mask. (**4a**) is the segmented image after using interactive thresholding, (**4b**) Segmented image after using top-hat, (**4c**) is the segmented image after the merger of (**4a**) and (**4b**), (**4d**) is the grayscale image before segmentation. (**5a**) displays the two-dimensional grayscale image, (**5b**) shows the two-dimensional threshold segmentation image, (**5c**) exhibits the two-dimensional rendering image, (**5d**) represents the components of the three-dimensional soil model, and (**5e**) showcases the complete three-dimensional soil model. Step (**6**) involves the analysis of pore angles within the soil).

- Quantitative analysis of pore characteristics

Porosity, a key indicator of soil physical properties, was quantitatively analyzed in this study. Using Avizo2019.1 software, two-dimensional slice porosity was calculated. This involved slicing the reconstructed pore model along the XY, XZ, and YZ planes and computing the ratio of the sum of pore pixels within each slice to the total projected area (Equation (1)), where A_0 represents the minimum pixel unit area (μm^2), and N denotes the number of pixels covering pores. The aspect ratio A_r, indicating the length-to-width ratio of the structural bodies [37], was calculated using L as the maximum particle length and W as the short side length. Notably, the 3D CT model's porosity was the average of the slice porosity. However, it is generally lower than the sample's actual porosity due to resolution constraints [38]. Pore size classification is based on the equivalent diameter, which equates to the diameter of a sphere of the same volume as the pore (Equation (2)) [21,25,39], where V_{3D} represents the volume of an individual pore.

$$A\left(\mu m^2\right) = N \times A_0\left(\mu m^2\right) \qquad (1)$$

$$EqDiameter(\mu m) = 3\sqrt{\frac{6 \times V_{3D}(\mu m^3)}{\pi}} \qquad (2)$$

The distribution of soil pores in both longitudinal and transverse directions was elucidated through the analysis of layered images obtained from segmented and binarized CT scans, as detailed in the 3D reconstruction process shown in Figure 3(5). Soil, being a typical natural porous medium, lacks a universally accepted definition for pore sizes [40]. Some studies have categorized pores based on size thresholds, using 0.5 μm and 50 μm as benchmarks. Pores between 0.5 and 50 μm are known to retain water, while those larger than 50 μm are crucial for air and water movement [41]. In this study, referring to the functional classification of pores in facilitating water movement and considering the actual resolution of CT scanning (14 μm), we have classified pores into two categories: water-retaining pores (WPs), ranging from 14–50 μm, and water-air regulating pores (WAPs), ranging from 50–8740.72 μm. The porosity of these pore types was calculated, yielding values for the volume of water-retaining pores (CTPW) and volume of water–air regulating pores (CTPWA). The difference between TP and CT-measured porosity (CTP) represents the porosity of soil pores smaller than 14 μm (P < 14 μm).

Furthermore, based on their connectivity to the soil network, the pores are classified as interconnected or isolated, depicted in blue and yellow, respectively, in Figure 3(5). Isolated pores, not connected to the main soil pore network, predominantly influence soil water retention. Conversely, interconnected pores, which are part of the network, significantly impact gas exchange and the movement of water and nutrients in the soil. The coordination number, indicating the number of pores connected to a single pore, suggests that a higher coordination number facilitates water and solute movement more efficiently t in the soil. The pore angle, defined as the angle between a pore's longest axis and the Z-axis, ranges from 0° to 90°, as demonstrated in Figure 3(6). Larger angles are generally less conducive

to the movement of water and solutes within a pore. All these parameters were extracted and analyzed using Avizo2019.1 software.

2.3.2. Soil Moisture Parameters

Soil bulk density (BD) was determined by the soil-cutting ring method. The bulk soil samples were dried at 105 °C in an oven until a constant weight was achieved. The BD value was calculated using the oven-dried weight and sample volume. Similarly, soil water parameters, including maximum water holding capacity (M_{axwc}), capillary water holding capacity (C_{pwc}), and field water holding capacity (FC), were also measured using the soil-cutting ring method [42]. Briefly, the original bulk soil samples were soaked in a container with water (note: the height of soaked water was slightly lower than the top of the cutting ring) for 24 h to ensure the soil was fully saturated by water and then weighed and denoted as m_1 (i.e., the weight of the cutting ring (m_0) plus the weight of the soil at this time). Then, these soaked samples were placed on quartz sand to remove gravity water and weighed afterward (note: the weight at this time was recorded as m_2). After removing the gravity water, these samples were left on the quartz sand for 2–5 days and then weighted again (note: the weight at this time was recorded as m_3). Finally, these samples were dried at 105 °C until a constant weight was achieved and then recorded the weight (m_4). Through the recorded weights, these water parameters, including M_{axwc}, C_{pwc} and FC, were calculated. Total soil porosity (TP) was also calculated according to the value of M_{axwc}.

The calculation of soil permanent wilting point (PWP) was obtained through measuring soil maximum hydroscopic water, which was determined by the saturated K_2SO_4 method [43]. Briefly, 10 g of air-dried soil (passed through a 2 mm sieve) was placed into a sealed desiccator containing saturated potassium sulfate, maintaining humidity at 98% and temperature at 20 °C for one week, then it was taken it out and weighed, then repeat weighing for 2–3 days until a constant weight is recorded (m_5). Then, place it in an oven at 105 °C to dry to a constant weight and record (m_6). Maximum effective water holding capacity (Mewc) was calculated according to the difference between WCm and PWP. The calculation equations of the parameters mentioned above are given below.

$$M_{axwc}(\%) = \frac{m_1 - m_0}{m_1 - m_4} \times 100$$

$$C_{pwc}(\%) = \frac{m_2 - m_0}{m_1 - m_4} \times 100$$

$$FC(\%) = \frac{m_3 - m_0}{m_3 - m_4} \times 100$$

$$TP(\%) = WC_m \times BD$$

$$PWP(\%) = \frac{m_5 - m_4}{m_4} \times 100$$

$$M_{ewc}(\%) = WC_m - PWP$$

Soil saturated hydraulic conductivity measurements were conducted using the KSAT saturated hydraulic conductivity meter (METER, Villingen, Germany). To assess the soil moisture evaporation rate, undisturbed soil samples were initially submerged in water, maintaining a 2 mm gap below the upper edge of the ring knife, until full saturation was achieved (indicated by a soil weight change of less than 0.1 g). The samples were then placed in a constant temperature oven set at 40 °C, creating a controlled environment with uniform temperature and humidity for the duration of the experiment. Soil weight was recorded at regular intervals. The soil moisture evaporation rate (EWC) was calculated by subtracting the current water content from the initial water content (IWC). Finally, the maximum effective soil moisture content was ascertained by calculating the difference between the field water-holding capacity and the soil permanent wilting point.

2.4. Statistical Analysis

The data were analyzed using SPSS software, version 19.0 (SPSS, Chicago, IL, USA). To compare the differences in pore and moisture parameters between the CCS and CFS samples, as well as among CCS samples with varying levels of pollution, the Mann–Whitney U test was utilized. This non-parametric test is suitable for independent samples. Additionally, the relationship between soil pore and moisture parameters was evaluated using Pearson's correlation coefficient (two-tailed). Statistical significance was established at a *p*-value of ≤0.05, indicating significant differences or correlations.

3. Results

3.1. Soil Pore Characteristics

3.1.1. Soil Porosity and Pore Number

Table 1 presents the differences in pore volume and pore number between the CFS and CCS samples. The TP and CTP in CCS are significantly lower than in CFS, with a statistically significant difference ($p < 0.05$). In contrast, for pores smaller than 14 μm (P < 14 μm), no significant difference is observed between CCS and CFS ($p > 0.05$). Furthermore, the CTPWA values in both CCS and CFS are similar to their respective CTP values. This indicates that coal pollution primarily reduces the CTPWA, which in turn decreases TP. Additionally, the total number of pores (CTN) in CCS is significantly lower than in CFS, accounting for only about 32% of the CFS value.

**Table 1.** Comparison of pore volume and pore number parameters between CCS and CFS.

	TP (%)	CTP (%)	P < 14 μm (%)	CTPW (%)	CTPWA (%)	CTN	CTNW/CTN (%)	CTNWA/CTN (%)
CFS	52.94 (1.10) A	23.23 (2.31) A	29.71 (0.41) A	0.01 (0.01) B	23.22 (0.03) A	7074.67 (1707.09) A	37.35 (1.16) B	62.65 (1.16) A
CCS	46.64 (1.67) B	13.79 (5.68) B	32.85 (5.02) A	0.23 (0.08) A	13.56 (0.74) B	2271.67 (756.99) B	55.08 (1.20) A	46.27 (1.20) B
3%-CCS	45.45 (1.55) a	15.28 (2.56) a	30.17 (1.37) a	0.26 (0.04) a	15.02 (1.46) a	2588.33 (119.64) a	53.76 (0.07) b	46.23 (0.07) a
4%-CCS	46.73 (1.08) a	14.49 (9.82) a	32.24 (8.74) a	0.29 (0.12) a	14.20 (5.60) a	2190.33 (1355.54) a	59.58 (1.35) a	40.42 (1.35) b
7%-CCS	47.50 (1.94) a	11.60 (3.88) a	35.90 (3.82) a	0.14(0.09) a	11.47 (2.25) a	2036.33 (443.80) a	57.33 (2.97) a	43.00 (2.97) b

Standard deviations are presented in parentheses. The symbols A and B indicate statistically significant differences between groups, while the symbols a and b denote significant differences within subgroups, with a *p*-value of <0.05.

Further analysis of the scanned pore numbers reveals that in CFS, the proportions of WPs and WAPs are 37% and 63%, respectively. In contrast, CCS shows a different distribution, with 55% WPs and 45% WAPs. These findings suggest that coal pollution considerably reduces the number of larger pores (particularly those exceeding 50 μm, classified as WAP), resulting in a shift in the soil pore structure from predominantly larger WAPs to smaller WPs and pores under 50 μm. When examining soils with varying levels of coal pollution, most pore parameters do not show significant differences. The only exceptions are the proportions of water-retaining pores (CTNW/CTN) and water–air regulating pores (CTNWA/CTN) between the 3%-CCS and the 4%-CCS teachers, as well as 7%-CCS samples. These exceptions highlight an increasing dominance of WP with rising levels of coal pollution.

3.1.2. Soil Pore Features Based on Two-Dimensional Slices

Figure 4 illustrates the changes in soil pore characteristics between CFS and CCS by displaying the proportional shifts in pore numbers within a 0.05 aspect ratio interval across three slicing planes (XY, XZ, and YZ). For CFS, the distribution of pore numbers across aspect ratios remains relatively consistent across these planes, predominantly ranging from 0.4 to 0.75, with the most significant peak observed between 0.7 and 0.75.
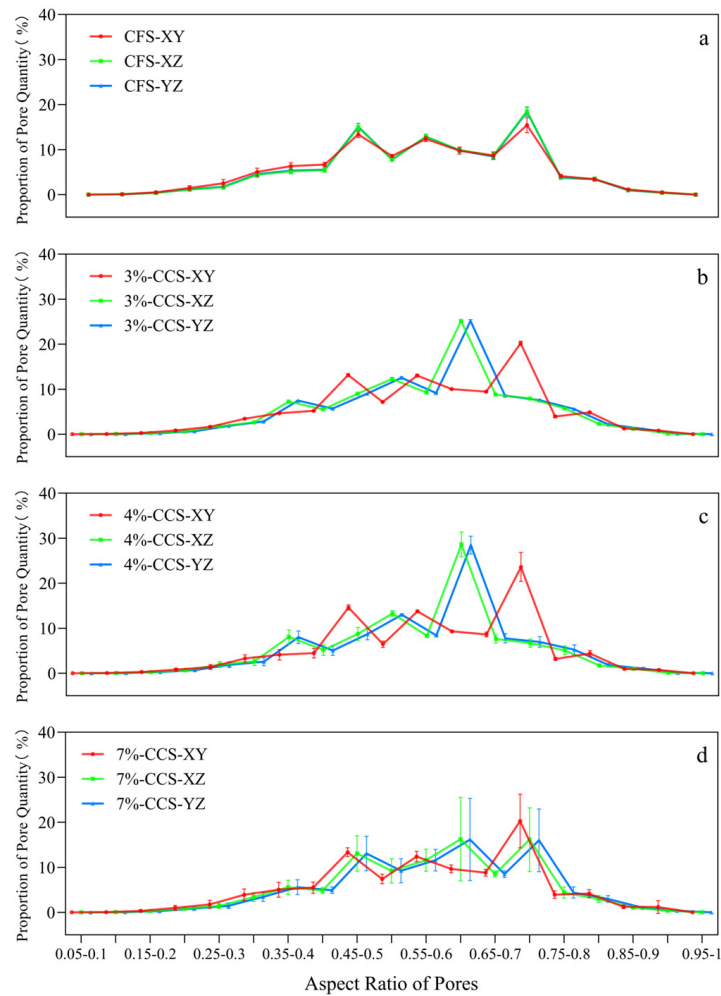
Figure 4. Proportional changes in the number of pores with different aspect ratios between CFS and CCS. (**a**–**d**) are the slice porosity of CCS, 3%-CCS, 4%-CCS, and 7%-CCS, respectively, within three slicing planes (XY, XZ, and YZ).

In contrast, coal pollution appears to maintain the distribution pattern in the XZ and YZ planes with no significant alterations in the concentration range. However, the peak ranges shift slightly to 0.6–0.65 in the XZ and YZ planes, while remaining at 0.7–0.75 in the XY plane, indicating a reduced peak range in the XZ and YZ planes for CCS. Notably, in CCS, the proportion of nearly circular pores (aspect ratio 0.5–0.75) increases by 4–8% on the Z-axis plane, while the proportion of elongated pores (aspect ratio 0.2–0.5) decreases by 4–6%. This suggests that coal pollution leads to a higher proportion of nearly circular pores along the Z-axis.

Figure 5 examines the changes in the aspect ratios of WPs and WAPs following exposure to coal pollution. After pollution exposure, the aspect ratio of WPs increases slightly by 0.003 to 0.017 along the Z-axis, while it decreases by 0.019 to 0.027 in the XY plane. For WAPs, the aspect ratio rises by 0.002 to 0.011 along the Z-axis and by 0.021 to 0.026 in the XY plane, with no significant changes in gradient correlating with the degree of coal pollution. These findings suggest that coal pollution causes soil pores to become flatter along the Z-axis, with WPs exhibiting greater deformation than WAPs.
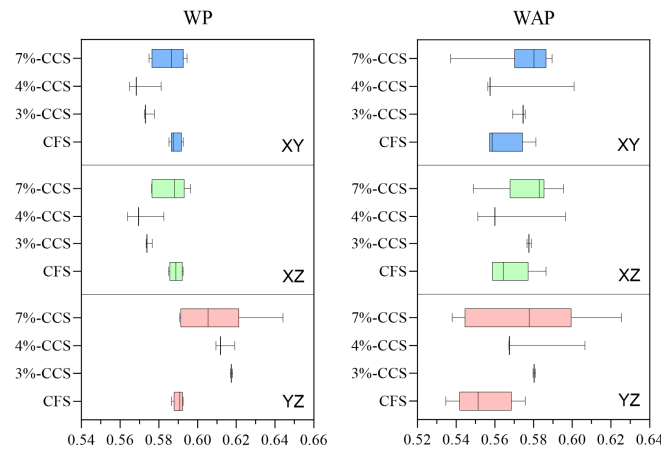
Figure 5. The distribution of mean aspect ratios of pores in CFS and CCS.

Figure 6 presents the pore distribution curves for slices in CFS and CCS. Across all directions, CFS demonstrates a higher pore volume compared to CCS. The coefficient of variation in slice pore volume for CCS ranges from 9% to 17% in the XY direction and from 4% to 19% in the YZ direction, both of which are higher than the range of 3% to 7% observed in CFS. However, in the XZ direction, the 7%-CCS shows a 7% lower coefficient of variation compared to CFS. This pattern indicates that coal pollution increases the heterogeneity of soil pores in the XY and YZ directions while reducing it in the XZ direction.
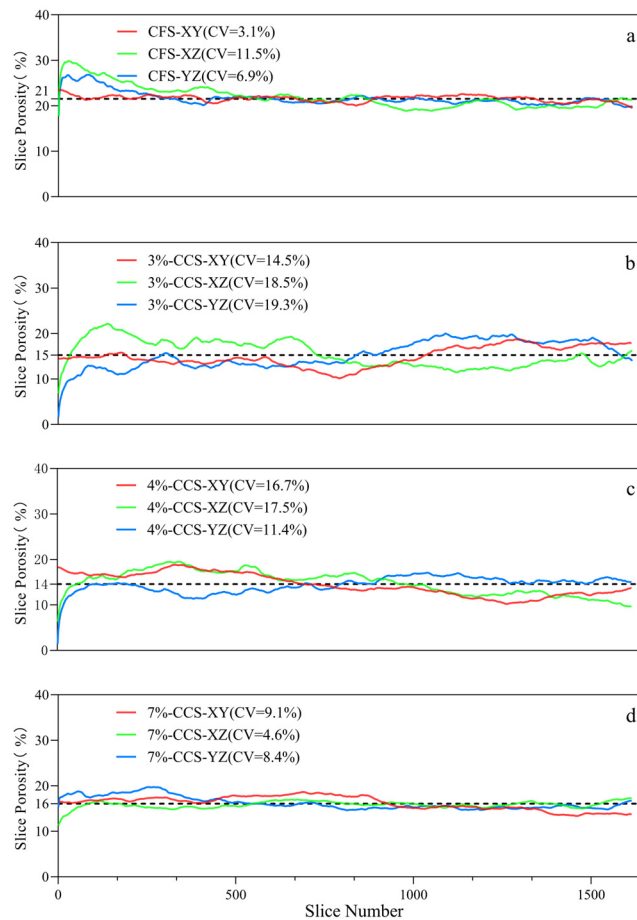
Figure 6. Pore volume of slices in CFS and CCS. (**a**), (**b**), (**c**) and (**d**) are the slicing well volumes of CCS, 3%-CCS, 4%-CCS, and 7%-CCS, respectively, within the three slice planes (XY, XZ, and YZ).The dotted line represents the average porosity.

3.1.3. Soil Pore Connectivity

Table 2 presents the connectivity properties and pore throat diameter distribution in CFS and CCS. Key parameters, including pore equivalent diameter (DP), isolated porosity ($P_{isolated}$), coordination number of interconnected pores (CN_{ic}), and interconnected porosity (P_{ic}), show no significant variation between CFS and CCS. In CFS, the values for the number of pore throats (N_{throat}), length of pore throats (L_{throat}), and inclination angle of interconnected pores (IA_{ic}) are 23,783, 7261, and 60, respectively. In contrast, CCS exhibits notable decreases in N_{throat} (7756) and L_{throat} (2039), along with an increase in IA_{ic} (65), indicating a statistically significant difference ($p < 0.05$). However, P_{ic}, N_{throat}, L_{throat}, and IA_{ic} do not significantly differ among soils, with varying levels of coal pollution ($p > 0.05$). This pattern suggests that coal pollution leads to an elevated IA_{ic} and a reduction in both N_{throat} and L_{throat}. Furthermore, as pollution levels increase, P_{ic} and CN_{ic} diminish, while $P_{isolated}$ increases.

Table 2. Isolated pore characteristics and interconnected pore parameters.

| | $P_{isolated}$ | P_{ic} | N_{throat} | L_{throat} (μm) | Distribution of Different Pore Throat Diameters (μm) | | | | | | CN_{ic} | IA_{ic} (°) | D_P (μm) |
					14–45	45–74	74–150	150–250	250–500	>500 μm			
CFS	0.44 (0.15) A	22.79 (2.16) A	23,783.33 (7731.57) A	7260.67 (1693.24) A	14.14 (3.61) A	16.02 (3.32) A	32.91 (3.60) A	20.29 (2.33) A	12.87 (5.26) B	3.77 (2.32) A	7.49 (1.87) A	59.73 (1.16) B	743.18 (337.45) A
CCS	0.60 (0.33) A	13.20 (5.92) A	7756.33 (3213.21) B	2038.78 (124.63) B	10.51 (1.70) A	11.74 (1.79) B	25.49 (2.74) B	21.72 (1.23) A	23.07 (3.97) A	7.47 (2.35) A	6.03 (0.63) A	64.55 (1.17) A	527.22 (54.99) A
3%-CCS	0.38 (0.10) b	14.91 (2.51) a	7761.00 (1125.63) a	2077.47 (30.56) a	11.19 (1.95) a	11.92 (2.23) a	25.83 (2.35) a	21.43 (0.13) a	22.69 (4.23) a	6.95 (2.17) a	6.27 (0.10) a	64.18 (0.91) a	550.43 (33.88) a
4%-CCS	0.60 (0.53) ab	13.89 (10.25) a	8247.33 (6036.11) a	1988.31 (211.07) a	10.14 (1.92) a	11.06 (2.35) a	23.83 (1.92) a	22.32 (1.42) a	25.18 (4.64) a	7.46 (0.51) a	6.23 (1.06) ab	64.88 (1.89) a	558.08 (61.46) a
7%-CCS	0.82 (0.07) a	10.79 (3.84) a	7260.67 (1693.24) a	2050.56 (101.84) a	10.21 (1.76) a	12.24 (1.08) a	26.80 (3.74) a	21.43 (1.81) a	21.34 (3.47) a	7.99 (4.03) a	5.58 (0.09) b	64.60 (0.84) a	473.14 (23.34) b

Standard deviations are provided in parentheses. Lowercase letters within the same column denote significant differences ($p < 0.05$). $P_{isolated}$ represents the isolated porosity, P_{ic} represents the interconnected porosity, N_{throat} represents the number of pore throats, L_{throat} represents the length of pore throats, CN_{ic} represents the coordination number of interconnected pores, and IA_{ic} represents the inclination angle of interconnected pores. The symbols A and B indicate statistically significant differences between groups, while the symbols a and b denote significant differences within subgroups, with a *p*-value of <0.05.

Figure 7 illustrates a marked rise in isolated pores in CCS. In CFS, the pore throat diameter predominantly clusters at 150 μm, highlighting a significant upsurge in pores smaller than 150 μm and a decrease in larger pores. Specifically, the proportion of pores within the 45–74 μm and 74–150 μm ranges in CFS is 16% and 33%, respectively. In CCS, there is a notable reduction in pores within these diameter ranges compared to CFS (12% and 25%, respectively; $p < 0.05$). Conversely, the proportion of pores within the 250–500 μm range in CCS increases from 13% to 25% ($p < 0.05$). No significant differences are observed in the pore throat diameter distribution across soils with different levels of coal pollution ($p > 0.05$), indicating that coal pollution decreases pore connectivity and reduces both the diameter and quantity of pore throats. In particular, it diminishes the proportion of smaller diameter soil pore throats while augmenting larger diameter throats.
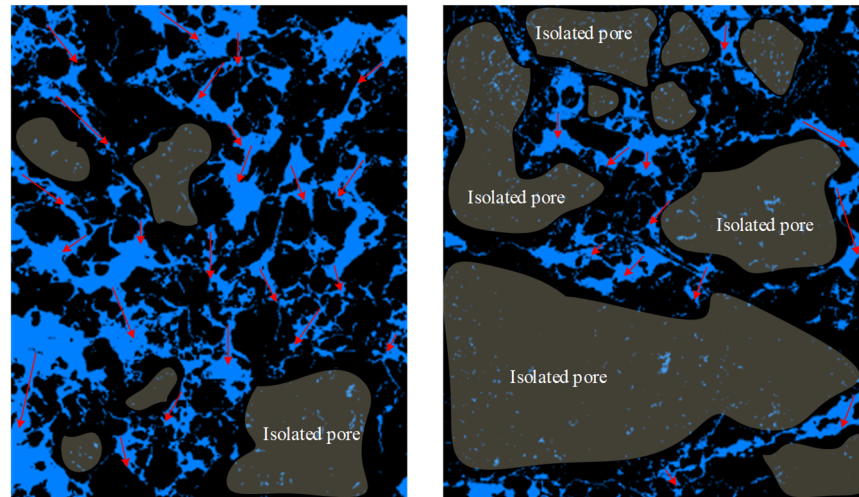
Figure 7. Schematic diagram illustrating the formation of isolated pores in coal-polluted soil. The left and right images display segmented representations of soil pores in CFS and CCS, respectively. The blue areas represent soil pores, the gray overlay indicates isolated pores, and the red arrows denote pathways for gas and water transport between pores.

Figure 8 illustrates the distribution of pore volume and quantity relative to IA_{ic} in 5° increments. Within the 45° to 90° range, CFS accounts for 74% of the volume proportion. In contrast, the proportion of soil pore angles in CCS varies from 81% to 83%. In the 10°–20° range, both the volume and quantity proportions of CCS soil pore angles are lower compared to those in CFS; however, these proportions increase in the 65°–70° and 85°–90° ranges. These results indicate that within the 45°–90° inclination angle spectrum, the volume proportion of pores exceeds 77%, with the quantity proportion surpassing 67%. Furthermore, coal pollution reduces the volume and quantity proportion of pore angles in the 10°–20° range, while promoting development in the 65°–70° and 85°–90° ranges.
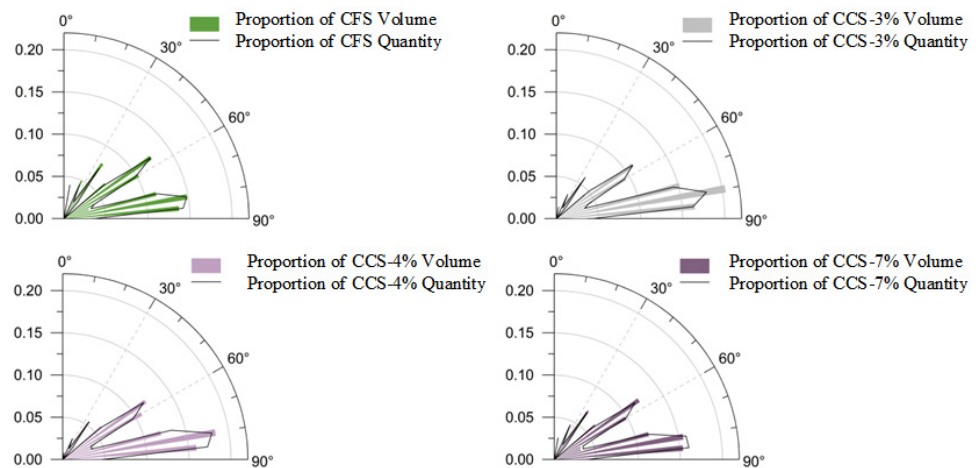
Figure 8. Proportion of pore angle quantity and volume in CFS and CCS.

3.2. Soil Moisture Characteristics

Table 3 presents the water characteristic parameters of CCS and CFS. In CCS, the saturation water content, permanent wilting point, and saturated hydraulic conductivity are measured at 38%, 7%, and 0.35, respectively. These values are significantly lower than those in CFS ($p < 0.05$). Conversely, both the field water holding capacity and maximum water holding capacity content in CCS significantly increase to 20% and 13%, respectively, compared with CFS. Among these parameters, variations are observed in the permanent wilting point, saturated hydraulic conductivity, and maximum water holding capacity

across soils with different levels of coal pollution. Meanwhile, field water holding capacity, capillary water holding capacity, and saturated hydraulic conductivity exhibit a gradient change, although these differences are not statistically significant. Overall, these results indicate that coal pollution reduces saturation water content, capillary water holding capacity, permanent wilting point, and saturated hydraulic conductivity, while enhancing field water holding capacity and maximum water holding capacity.

Table 3. Moisture characteristics of CCS and CFS.

	Maximum Water Holding Capacity (%)	Capillary Water Holding Capacity (%)	Field Capacity (%)	Soil Permanent Wilting Point (%)	Maximum Water Holding Capacity (%)	Saturated Hydraulic Conductivity (cm/h)
CFS	44.10 (5.22) A	33.37 (1.23) A	19.64 (0.18) B	8.20 (0.32) A	11.41 (0.55) B	1.03 (0.28) A
CCS	37.51 (2.84) B	32.28 (2.23) A	20.45 (0.67) A	7.48 (0.47) B	12.91 (0.84) A	0.35 (0.22) B
3%-CCS	37.38 (4.01) a	32.69 (0.89) a	20.47 (0.50) a	7.13 (0.28) b	13.27 (0.45) a	0.55 (0.19) a
4%-CCS	37.40 (2.11) a	32.54 (3.56) a	20.16 (0.86) a	7.99 (0.36) a	12.02 (0.61) b	0.40 (0.09) a
7%-CCS	37.75 (2.59) a	31.61 (1.60) a	20.71 (0.59) a	7.30 (0.19) b	13.43 (0.70) a	0.11 (0.05) b

The symbols A and B indicate statistically significant differences between groups, while the symbols a and b denote significant differences within subgroups, with a *p*-value of <0.05.

Figure 9 illustrates the dynamics of water evaporation rates for both CCS and CFS, ranging from water saturation to air-dry conditions. During the initial 22 h, which corresponds to 0.83–0.90 times the saturation water content, the evaporation rates for both CCS and CFS exhibit similar fluctuating patterns. However, after 22 h and extending up to 250 h, the evaporation rates for all CCS groups consistently remain lower than those of CFS. This trend indicates that coal pollution may reduce the soil water evaporation rate to some extent.
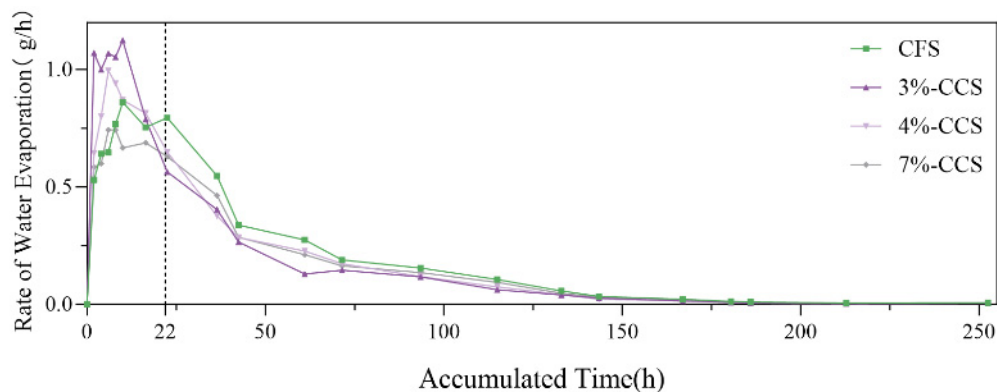
Figure 9. Water evaporation rates of soil with and without coal pollution.

3.3. The Connection between Soil Pores and Moisture

Pearson's correlation analysis, as shown in Figure 10, reveals consistent correlation trends between soil pore parameters and moisture characteristics. Key moisture parameters, including maximum water holding capacity, capillary water holding capacity, soil permanent wilting point, and saturated hydraulic conductivity, demonstrate parallel correlation trends with various pore parameters. These moisture parameters exhibit positive correlations with specific pore metrics (DP, TP, CTP, P_{ic}, CTPWA), pore quantity parameters (CTN, CTNWA/CTN), pore throat characteristics, and the proportion of throats with diameters smaller than 150 μm, as well as with CN_{ic}. Notably, CTN displays a significant positive correlation with all four moisture parameters.
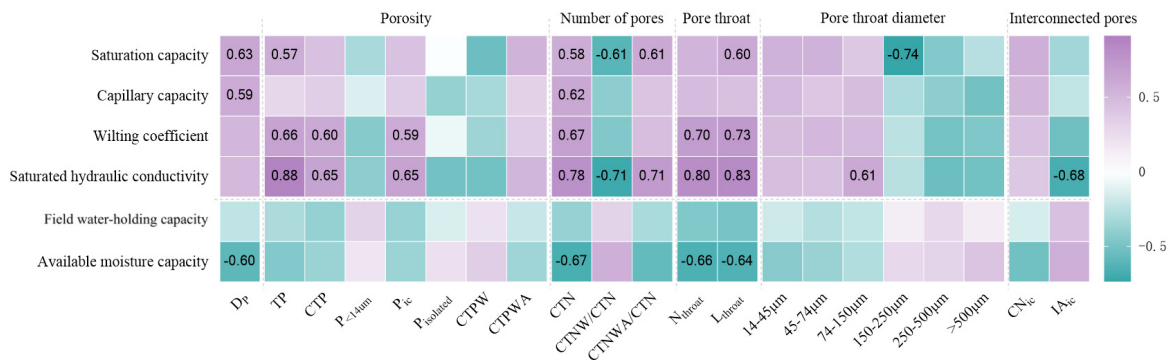
Figure 10. Correlation analysis between soil pore characteristics and moisture properties (No numbers indicate non-significant correlations).

Conversely, the proportion of pore throats within the 150–250 μm diameter range shows a strong negative correlation with maximum water holding capacity, indicated by a correlation coefficient (r) of −0.74. In contrast, field water-holding capacity and maximum effective water content demonstrate divergent correlation trends with pore parameters. Field water-holding capacity shows negligible correlations with pore parameters, while maximum effective water content exhibits significant negative correlations with DP, CTN, N_{throat}, and L_{throat}. Among these, CTN has the most pronounced correlation with maximum effective water content (r = −0.67).

In summary, the findings from Sections 3.1 and 3.2 indicate that increased coal pollution broadly affects soil pore parameters, particularly impacting saturated hydraulic conductivity, TP, CTN, and pore throat metrics. These pore characteristics significantly influence the soil's moisture properties.

4. Discussion

4.1. Impact of Coal Pollution on Soil Pores

The variation process of soil pores in farmland soil is the result of both natural and human factors. Among the natural factors, rainfall has the most significant influence. During rainfall, both the dispersal effect of raindrop splashing and the infiltration process can affect the distribution of soil pores [44]. Human factors such as tillage practices [45,46], fertilization methods [47], and crop root systems [48,49] also play a role in the changes in soil pore distribution. The environmental conditions in our study area were consistent, with uniform tillage practices and crops, ensuring that coal pollution was the primary influencing factor. This study reveals significant alterations in soil pore parameters due to coal pollution, which can be attributed to both the filling and clogging effects of coal particles. The term "filling" refers to the intrusion of coal particles into soil pores, thereby occupying the pore space. In contrast, "clogging" involves the partitioning of soil pore space resulting from interactions between the coal particles and the other substances in the soil.

A marked decrease in soil porosity parameters, such as TP and CTP, is observed in the presence of coal pollution. This reduction is primarily due to the filling effect, where smaller coal particles, particularly those under 45 μm—comprising 66% of particles in CCS—penetrate larger soil pores. Their low porosity allows them to occupy significant pore space, leading to decreased TP and CTP. This finding is consistent with existing research on the impact of fine particle organic carbon addition on soil porosity [50,51].

Furthermore, coal pollution results in a notable decrease in the number of pore throats within the 14–150 μm diameter range, as evidenced by reductions in N_{throat}, CN_{ic}, and L_{throat}, and an increase in $P_{isolated}$. This phenomenon can be attributed to the clogging effect of coal particles. During irrigation, fine coal particles migrate with moisture into WAPs and clog them, causing significant reductions in CTPWA and CTNWA/CTN. The pore and throat classification performed using Avizo software, based on the maximum ball

algorithm [52], suggests that coal particles, being similar in size to pore throats, effectively block these throats. This blockade results in the formation of numerous isolated pores and contributes to the observed decreases in N_{throat}, CN_{ic}, L_{throat}, along with an increase in $P_{isolated}$, as illustrated in Figure 7.

Further examination of pore throat morphology in two-dimensional slices elucidates the post-infiltration effects of coal particles on soil. The clogging effect causes pore throats within the 14–150 μm range to fracture into multiple isolated pores, while the bottoms of larger pores become filled with coal particles. These combined effects alter the shape of the pores in CCS, making them more circular and flattened along the Z-axis. Notably, WPs exhibit more pronounced flattening compared to WAPs. Additionally, the average pore size in CCS decreases across all planes, with the 7%-CCS showing relatively minor changes, indicating a state of balance in the action of coal particles and resulting in a more gradual change in average pore size.

Interestingly, the varying degrees of coal pollution (within the 3–7% range) do not significantly affect certain soil pore parameters (TP, CTP, P < 14 μm, CTPW, and CTPWA), indicating that changes in the quantity of coal particles have a less pronounced impact on soil pore volume within this range. However, differences in coal particle quantity significantly impact CTNW/CTN and CTNWA/CTN. This indicates that as coal pollution increases, the clogging effect intensifies, leading to a shift from water–air regulating pores and throats within the 14–150 μm range towards WPs.

4.2. Impact of Coal Pollution on Soil Moisture

Soil moisture dynamics are intricately linked to soil pore characteristics, including porosity, morphology, size, complexity, and connectivity, all of which are crucial for the supply, retention, and transport of moisture in soil [53]. The observed changes in soil moisture parameters due to coal pollution can be traced back to modifications in soil pore properties, influenced by the filling and clogging effects of coal particles.

Saturation water content in soil, which indicates maximum water holding capacity, is generally enhanced by materials with a rich pore structure and larger particles, such as biochar and gasifier slag [54,55]. In contrast, our study finds that the presence of coal particles, characterized by low porosity and smaller size, results in a significant decrease in maximum water holding capacity. This decrease is primarily attributed to a reduction in soil bulk density, a decline in CTN, and a decrease in TP. The lower saturation water content in CCS reflects a diminished maximum water holding capacity due to coal pollution, necessitating adjustments in irrigation volume to prevent water waste and soil saturation.

Capillary water holding capacity also shows a notable decrease in CCS, aligning with reduction in CTN and bulk density. Since capillary action is largely driven by the surface tension between soil particles and pores, a reduced CTN can impede this process. While smaller pore diameters typically facilitate capillary action, the obstruction of pore spaces by coal particles limits the effective pore space available for water transport, ultimately leading to the observed decrease in capillary water holding capacity.

Field water holding capacity and soil moisture evaporation rate are key indicators of soil water retention ability. In CCS, there is a notable increase in field water holding capacity accompanied by a decrease in moisture evaporation rate. While additives such as compost, coco peat, earthworm castings, and biochar are known to enhance soil water retention due to their hydrophilic properties and porous structure [55], coal particles do not exhibit these characteristics. Instead, the observed increase in water retention in CCS can be attributed to alterations in the pore structure, including reduced pore volume (TP, capillary porosity, total porosity of water-filled pores) and increased isolated pores ($P_{isolated}$). These modifications suggest a diminished space for water transport while expanding the capacity for water storage.

Additionally, decreases in L_{throat}, N_{throat}, and CN_{ic} restrict water movement within the soil. The transformation of pore morphology towards more rounded and flattened shapes

along the Z-axis, along with an increase in IA_{ic}, further contributes to water retention and accumulation, thereby enhancing soil water retention capacity.

The soil permanent wilting point, which indicates a soil's drought resistance capability [56], significantly decreases in CCS. This change correlates with reductions in TP, CTN, capillary porosity, and L_{throat}. Moreover, the decline in P_{ic} and L_{throat} suggests an increased propensity for pores to store water. A decrease in N_{throat} in CCS also limits water evaporation, resulting in a lowered soil permanent wilting point and indicating improved drought resistance.

The maximum effective water content, representing the upper limit of soil water that most plants can utilize, also increases in CCS. This increase is attributed to decreases in CTN, bulk density, L_{throat}, and N_{throat}, which collectively slow down water movement within the soil and prolong water retention. The resulting rise in field water holding capacity and drop in soil permanent wilting point contribute to an elevated maximum effective water content.

In conclusion, coal pollution appears to enhance soil moisture characteristics, predominantly through the mechanisms of coal particle filling and clogging within soil pores.

4.3. Potential Impact of Coal Pollution on Soil Microecology

Soil pores play a crucial role in shaping the microenvironment of the soil, directly controlling the movement of microorganisms and influencing the composition and diversity of microbial communities. First, coal pollution has certain effects on the physicochemical properties of soil. Abramowicz et al. reported that nearly 40% of soil sampling points in coal waste accumulation areas exhibited acidic conditions [57,58], mainly driven by mineral decomposition and increased microbial activity [59]. Coal particles, characterized by their black color and strong light absorption, reduce infrared reflectance at lower temperatures, thereby increasing the specific heat capacity and thermal conductivity of the soil, leading to enhanced energy absorption. Water has a specific heat capacity of 4.18 J/g·°C, significantly higher than that of soil (0.8–1.5 J/g·°C) [60], which allows for coal-contaminated soil (CCS) to retain heat further under strong water retention capacity. Studies have shown that soil total porosity (TP) and air-filled porosity (AP) are typically higher in summer than in winter [61], indicating that temperature affects TP and AP levels and promotes nitrogen cycling [62]. Although higher pH values slow down the decomposition of plant-derived molecules, lower pH values can enhance nitrogen availability [63]. The BET adsorption tests show that coal particles have smaller specific surface areas and poorer adsorption capacity, leading to reduced soil nitrogen and phosphorus adsorption capacity, thereby increasing the availability of these nutrients. These changes in the physicochemical properties of the soil affect, to some extent, the living environment of soil microorganisms. Meanwhile, soil pores indirectly provide gases and liquids for microbial activity, thereby influencing microbial functions [64,65]. Soil porosity characteristics not only regulate the diffusion of water and gases but also affect the movement of chemicals and microbial activity, which in turn influence the decomposition of exogenous substrates such as plant residues [66]. For example, Juarez et al. [67] found that in areas affected by pore structures (such as pores < 1 μm or soil particle surfaces), the decomposition rate of "old" soil organic carbon is faster, a phenomenon known as the "priming effect." The distribution and combination of soil pores are key factors influencing the occurrence and intensity of the priming effect [68,69].

In CCS, the increase in isolated pores restricts the range of microbial activity, which may significantly enhance microbial diversity in these areas [70]. Additionally, the distribution and activity of microorganisms in the soil are influenced not only by pore size but also by pore connectivity and aeration [71,72]. For instance, Negassa et al. [73] used CT scanning and DNA sequencing techniques to study samples with added plant residues, finding that larger pores primarily hosted cellulose-decomposing bacteria (Bacteroidetes, Proteobacteria, Actinobacteria, and Firmicutes), while smaller pores were mainly occupied by oligotrophic Acidobacteria. Contrary to CFS, the poorer pore connectivity in CCS may

lead to significant changes in microbial types. Therefore, changes in soil pore characteristics caused by coal pollution affect the composition and diversity of soil microorganisms.

To better address these changes, research has also begun to focus on the broader impact of coal pollution on agricultural ecosystems. Our study provides new insights into the soil pollution problems in areas affected by coal production and crop intercropping. While previous studies have shown that industrial pollution significantly impacts soil health by altering soil structure [74], nutrient availability [75], and microbial activity [76], the impact of coal pollution, especially in coal–crop intercropping areas, remains underexplored. The unique conditions in the Jiaozuo region allow our research to fill this gap, revealing how coal particles affect soil structure and moisture characteristics. Additionally, our research aligns with global efforts to promote agricultural sustainability in polluted environments [77]. Similar studies in other coal-producing regions, such as the Appalachian region of the United States [78], have also found soil health issues and declining agricultural yields. This highlights the need for targeted remediation strategies in coal-contaminated areas, such as phytoremediation, bioaugmentation, and soil amendments.

Throughout the entire growth period of wheat, we observed an intriguing phenomenon, where the growth of CCS before the seedling stage was significantly better than that of CFS, yet the yield of CCS was approximately 10% lower than that of CFS. The changes in pore structure in CCS provide a water advantage that enhances the soil's specific heat capacity during the low-temperature period before the seedling stage. Coupled with its darker color, which aids in increasing temperature, this advantage in water and temperature allows microorganisms to decompose straw more rapidly before the seedling stage, thereby providing essential nutrients for the plants. However, this advantage diminishes as temperatures rise after the seedling stage. At this point, CCS is unable to provide additional nutrients due to the rapid decomposition of straw earlier, resulting in reduced yield. Long-term coal pollution has altered soil structure, indicating that timely post-seedling fertilization measures may enhance production in CCS. Continuous monitoring and research into restoration strategies and field management—including plant remediation, bio-enhancement, soil improvement, and fertilizing methods such as nitrogen fertilizer postponing application—are recommended to optimize productivity in coal-contaminated soils.

5. Conclusions

This study investigates the effects of coal pollution on soil pore and moisture characteristics, utilizing CT scanning technology and soil moisture measurements to elucidate these complex interactions. The findings indicate that coal pollution significantly reduces soil pore space, as evidenced by decreases in TP and CTP. Notably, the parameters associated with water-accessible pores, such as CTPWA and CTNWA/CTN, also decline. In contrast, parameters linked to water-occupied pores, including CTPW and CTNW/CTN, exhibit an increase.

Coal pollution is found to cause significant fracturing in pores within the 14–150 μm diameter range, resulting in the formation of numerous isolated pores. Consequently, N_{throat}, L_{throat}, and the quantity of pores smaller than 150 μm decrease, while $P_{isolated}$ and the number of pores larger than 150 μm increase. The morphology of soil pores transforms, becoming more rounded and exhibiting a flattened profile along the Z-axis, accompanied by an increase in IA_{ic}. Furthermore, the study identifies increased heterogeneity in soil pores in the XY and YZ directions, contrasting with a reduction in the XZ direction.

In terms of soil moisture characteristics, coal pollution leads to decreased maximum water holding capacity, soil permanent wilting point, saturated hydraulic conductivity, and capillary water holding capacity. However, it simultaneously enhances the soil's water retention ability. The study attributes the influence of coal pollution on soil pore parameters to the dual effects of coal particles filling and clogging the pores. Similarly, the impact on soil moisture parameters is predominantly realized through these mechanisms, highlighting the significant role of coal particle interaction in altering soil hydrological properties.

Abbreviations

Abbreviation	Full Name
TP	Total porosity
CTP	CT-measured porosity
CTNW/CTN	Proportion of water-retaining pores
CTPW	Volume of water-retaining pores
CTNWA/CTN	Proportion of water-air regulating pores
CTPWA	Volume of water-air regulating pores
CN_{ic}	Coordination number of interconnected pores
IA_{ic}	Inclination angle of interconnected pores
N_{throat}	Number of pore throats
L_{throat}	Length of pore throats
P_{ic}	Interconnected porosity
$P_{isolated}$	Isolated porosity
WP	Water-retaining pore
WAP	Water-air regulating pore
$P < 14\ \mu m$	Porosity (d < 14 μm)
CTN	Number of pores
DP	Pore equivalent diameter

References

1. Hu, Z.; Li, J.; Zhao, Y. Problems, Reasons and Countermeasures for Environmental Quality and Food Safety in the Overlapped Areas of Crop and Mineral Production. *Sci. Technol. Rev.* **2006**, *24*, 93–94.
2. Nie, X.; Zhao, T.; Su, Y. Fossil fuel carbon contamination impacts soil organic carbon estimation in cropland. *Catena* **2021**, *196*, 104889. [CrossRef]
3. Yunusa, I.; Eamus, D.; Desilva, D.L. Fly-ash: An exploitable resource for management of Australian agricultural soils. *Fuel* **2006**, *85*, 2337–2344. [CrossRef]
4. Jankowski, J.; Ward, C.R.; French, D.; Groves, S. Mobility of trace elements from selected Australian fly ashes and its potential impact on aquatic ecosystems. *Fuel* **2006**, *85*, 243–256. [CrossRef]
5. Zhao, S.W.; Zhao, Y.G.; Wu, J.S. Quantitative analysis of soil pores under natural vegetation successions on the Loess Plateau. *Sci. China Earth Sci.* **2010**, *53*, 617–625. [CrossRef]
6. Song, M.; Lin, S.; Takahashi, F. Coal fly ash amendment to mitigate soil water evaporation in arid/semi-arid area: An approach using simple drying focusing on sieve size and temperature. *Resour. Conserv. Recycl.* **2020**, *156*, 104726. [CrossRef]
7. Wang, J.; Li, X.; Bai, Z.; Huang, L. The effects of coal gangue and fly ash on the hydraulic properties and water content distribution in reconstructed soil profiles of coal-mined land with a high groundwater table. *Hydrol. Process.* **2017**, *31*, 687–697. [CrossRef]
8. Zhang, Y.; Qi, X.; Zou, J.; Rao, Y.; Chen, L.; Zhang, L.; Ji, Y.; Liang, Z. Effects of water immersion on the pore structure and thermodynamic properties of coal gangue. *Fuel* **2023**, *346*, 128273. [CrossRef]
9. Chen, M.; Chen, X.Y.; Wang, X.G.; Zhang, L.X.; Zhang, D.; Zhu, J.M. Variation of water and air in reconstruction soil profile and its response to temperature gradient in coal mine area. *J. Coal Sci. Eng. (China)* **2021**, *46*, 1309–1319. [CrossRef]
10. Fujikawa, T.; Miyazaki, T. Effects of Bulk Density and Soil Type on the Gas Diffusion Coefficient in Repacked and Undisturbed Soils. *Soil Sci.* **2005**, *170*, 892–901. [CrossRef]

11. Guo, J.; Dan, Z.; Chen, W.; Abdulazeam, S. Experiment research on improving the covering soil of open-pit mine tailings pond with coal slurry. *Coal Sci. Technol.* **1998**, 45–49.
12. Yu, M.; van Der Ploeg, M.; Ma, X.; Ritsema, C.J.; Geissen, V. Effects of microplastics and earthworm burrows on soil macropore water flow within a laboratory soil column setup. *Vadose Zone J.* **2021**, *19*, e20059. [CrossRef]
13. Liu, M.; Wu, D.; Wu, S.; Liao, L. Characteristic of soil macropores under various types of forest coverage andtheir influence on saturated hydraulic conductivity in the Three GorgesReservoir Area. *Acta Ecol. Sin.* **2016**, *36*, 3189–3196.
14. Qiao, Z.; Cao, Y.; Liu, L.; Wang, J.; Cui, J.; Xu, H.; Abdulazeam, S. Analysis of slurry characteristics and sedimentation influencing factors in Zhunneng Coal Preparation Plant. *Coal Process. Compr. Util.* **2020**, *4*, 1–4+8. [CrossRef]
15. Yu, H.; Dong, Z.; Yang, J.; Liu, R.; Cao, N.; Bi, B.; Bi, Y.; Abdulazeam, S. Study on soil macropore characteristics and infiltration capacity of differentland use types based on CT scanning. *J. Arid Land Resour. Environ.* **2023**, *37*, 55–61.
16. Pires, L.F.; Cooper, M.; Cássaro, F.A.M.; Reichardt, K.; Bacchi, O.O.S.; Dias, N.M.P. Micromorphological analysis to characterize structure modifications of soil samples submitted to wetting and drying cycles. *Catena* **2008**, *72*, 297–304. [CrossRef]
17. Zeng, Z.; Kong, L.; Wang, M.; Sayem, H.M. Assessment of engineering behaviour of an intensely weathered swelling mudstone under full range of seasonal variation and the relationships among measured parameters. *Can. Geotech. J.* **2018**, 1837–1849. [CrossRef]
18. Wan, Y.; Xue, Q.; Liu, L. Study on the permeability evolution law and the micro-mechanism of CCL in a landfill final cover under the dry-wet cycle. *Bull. Eng. Geol. Environ.* **2014**, *73*, 1089–1103. [CrossRef]
19. Zhang, X.W.; Kong, L.W.; Cui, X.L.; Yin, S. Occurrence characteristics of free iron oxides in soil microstructure: Evidence from XRD, SEM and EDS. *Bull. Eng. Geol. Environ.* **2016**, *75*, 1493–1503. [CrossRef]
20. Yang, C.; Liu, J.; Lu, S. Pyrolysis temperature affects pore characteristics of rice straw and canola stalk biochars and biochar-amended soils. *Geoderma* **2021**, *397*, 115097. [CrossRef]
21. Liu, B.; Ma, R.; Fan, H. Evaluation of the impact of freeze-thaw cycles on pore structure characteristics of black soil using X-ray computed tomography. *Soil Tillage Res.* **2021**, *206*, 104810. [CrossRef]
22. Rogers, E.D.; Monaenkova, D.; Mijar, M.; Nori, A.; Goldman, D.I.; Benfey, P.N. X-ray computed tomography reveals the response of root system architecture to soil texture. *Plant Physiol.* **2016**, *171*, 2028–2040. [CrossRef] [PubMed]
23. Capowiez, Y.; Sammartino, S.; Keller, T.; Bottinelli, N. Decreased burrowing activity of endogeic earthworms and effects on water infiltration in response to an increase in soil bulk density. *Pedobiologia* **2021**, *85–86*, 150728. [CrossRef]
24. Zhu, H.; Zhang, Y.; Li, Z.; Xue, X. Study on Crack Development and Micro-Pore Mechanism of Expansive Soil Improved by Coal Gangue under Drying–Wetting Cycles. *Materials* **2021**, *14*, 6546. [CrossRef]
25. Feng, Y.; Wang, J.; Liu, T.; Bai, Z.; Reading, L. Using computed tomography images to characterize the effects of soil compaction resulting from large machinery on three-dimensional pore characteristics in an opencast coal mine dump. *J. Soil Sediments* **2019**, *19*, 1467–1478. [CrossRef]
26. Ferreira, T.R.; Archilha, N.L.; Pires, L.F. An analysis of three XCT-based methods to determine the intrinsic permeability of soil aggregates. *J. Hydrol.* **2022**, *612*, 128024. [CrossRef]
27. Min, X.; Dong, Z.; Bo, H.; Zheng, G.; Li, Q.; Chang, X.; Li, X. Alternative Soil Substrates Addition Cause Deterioration in Reclaimed Soil Macropore Networks at Eastern Mining Area, China. *Sustainability* **2022**, *14*, 10519. [CrossRef]
28. An, R.; Kong, L.; Zhang, X.; Li, C. Effects of dry-wet cycles on three-dimensional pore structure and permeability characteristics of granite residual soil using X-ray micro computed tomography. *J. Rock Mech. Geotech. Eng.* **2022**, *14*, 851–860. [CrossRef]
29. Cheng, J.; Nie, X.; Liu, C. Spatial variation of soil organic carbon in coal-mining subsidence areas. *J. China Coal Soc.* **2014**, *39*, 2495–2500.
30. Rumpel, C.; Balesdent, J.; Grootes, P.; Weber, E.; Gel-Knabner, I.K. Quantification of lignite- and vegetation-derived soil carbon using 14C activity measurements in a forested chronosequence. *Geoderma* **2003**, *112*, 155–166. [CrossRef]
31. Ussiri, D.A.N.; Lal, R. Method for Determining Coal Carbon in the Reclaimed Minesoils Contaminated with Coal. *Soil Sci. Soc. Am. J.* **2008**, *72*, 231–237. [CrossRef]
32. Chabbi, A.; Rumpel, C.; Grootes, P.M.; Mariotti, A. Isotopic tracers for the analysis of vegetation-derived organic matter in lignite-containing soils and sediments along a transect ranging from a forest soil to submerged lake sediment. *Org. Geochem.* **2006**, *37*, 740–753. [CrossRef]
33. Nie, X.J.; Liu, X.; Sun, Y.T.; Xie, F.F.; He, J.; Gao, S. Effect of Coal Accumulation on Soil Aggregate Structure in the Mine-crop Overlapped Zone. *J. Soil Water Conserv.* **2019**, *33*, 169–175. [CrossRef]
34. Taina, I.A.; Heck, R.J.; Elliot, T.R. Application of X-ray computed tomography to soil science: A literature review. *Can. J. Soil Sci.* **2008**, *88*, 1–19. [CrossRef]
35. Kumar, S.; Anderson, S.H.; Udawatta, R.P.; Gantzer, C.J. CT-measured macropores as affected by agroforestry and grass buffers for grazed pasture systems. *Agroforest. Syst.* **2010**, *79*, 59–65. [CrossRef]
36. Ko, S.J.; Lee, Y.H. Center weighted median filters and their applications to image enhancement. *IEEE Trans. Circuits Syst.* **1991**, *38*, 984–993. [CrossRef]
37. Wang, R.; Li, J.; Zhang, J. Grain shape analysis of calcareous soil. *Rock Soil Mech.* **2005**, 1389–1392. [CrossRef]
38. Li, X.; Lu, Y.; Zhang, X.; Lu, Y.; Yang, Y. Pore-fissure ldentification and Characterization of Paleosol Based on X-rayComputed Tomography. *Bull. Soil Water Conserv.* **2018**, *38*, 224–230.

39. Capowiez, Y.; Sammartino, S.; Michel, E. Using X-ray tomography to quantify earthworm bioturbation non-destructively in repacked soil cores. *Geoderma* **2011**, *162*, 124–131. [CrossRef]
40. Christensen, B.T. Physical fractionation of soil and structural and functional complexity in organic matter turnover. *EJSS* **2001**, *52*, 345–353. [CrossRef]
41. South Eastern Kenya University. DAS 101: Principles of Soil Physics. 2017. Available online: http://repository.seku.ac.ke/handle/123456789/5959 (accessed on 27 February 2020).
42. Shidan, B. *Analysis of Soil Agricultural Chemistry*; China Agriculture Press: Beijing, China, 2000; ISBN 7109066444.
43. *GB 7836-1987*; Determination of Forest Soil Maximum Hygroscopicity. Code of China: Beijing, China, 1988.
44. Marshall, T.J. A relation between permeability and size distribution of pores. *J. Soil Sci.* **1958**, *9*, 1–8. [CrossRef]
45. Edwards, W.M.; Shipitalo, M.J.; Traina, S.J.; Edwards, C.A.; Owens, L.B. Role of lumbricus terrestris (L.) burrows on quality of infiltrating water. *Soil Biol. Biochem.* **1992**, *24*, 1555–1561. [CrossRef]
46. Da Veiga, M.; Horn, R.; Reinert, D.J.; Reichert, J.M. Soil compressibility and penetrability of an Oxisol from southern Brazil, as affected by long-term tillage systems. *Soil Tillage Res.* **2007**, *92*, 104–113. [CrossRef]
47. Bronick, C.J.; Lal, R. Soil structure and management: A review. *Geoderma* **2005**, *124*, 3–22. [CrossRef]
48. Dal Ferro, N.; Sartori, L.; Simonetti, G.; Berti, A.; Morari, F. Soil macro- and microstructure as affected by different tillage systems and their effects on maize root growth. *Soil Tillage Res.* **2014**, *140*, 55–65. [CrossRef]
49. Martin, S.L.; Mooney, S.J.; Dickinson, M.J.; West, H.M. The effects of simultaneous root colonisation by three Glomus species on soil pore characteristics. *Soil Biol. Biochem.* **2012**, *49*, 167–173. [CrossRef]
50. Tian, D. The Experimental Study of Influence of Biochar on DifferentTexture Soils Structure and Hydraulic Characteristic Parameters. Master's Thesis, Inner Mongolia Agricultural University, Hohhot, China, 2013.
51. Yan, C.; Hong, M.; Qin, J.; Fu, J.; Li, H.; Wang, Y. Effects of biochar on hydraulic characteristics of aeolian sandy soil in Hetian. *Agric. Res. Arid Areas* **2021**, *39*, 21–28.
52. Denney, D. Robust Determination of the Pore-Space Morphology in Sedimentary Rocks. *J. Pet. Technol.* **2004**, *56*, 69–70. [CrossRef]
53. Rabot, E.; Wiesmeier, M.; Schlüter, S.; Vogel, H.J. Soil structure as an indicator of soil functions: A review. *Geoderma* **2018**, *314*, 122–137. [CrossRef]
54. Wang, J.; Huang, C.; Feng, S.; Liu, C.; Li, H.; Han, Q. Using Biochar Amendment to lmprove the Physicochemical Properties of Soil in Coastal Tidal Area. *J. Irrig. Drain.* **2022**, *41*, 125–130. [CrossRef]
55. Yin, C.; Zhao, J.; Liu, X.; Yu, Z.; Liu, H. Effect of Coal Water Slurry Gasification Slag on Soil Water Physical Characteristics and Properties in Saline-Alkali Soil Improvement. *J. Sens.* **2022**. [CrossRef]
56. Qiao, Z. Study on the influence factors of wilting point. *J. Water Resour. Water Eng.* **2008**, *2*, 82–84.
57. Wei, Y.Q.; Zhao, Y.; Lu, Q.; Cao, Z.; Wei, Z. Organophosphorus-degrading bacterial community during composting from different sources and their roles in phosphorus transformation. *Bioresource Technol.* **2018**, *264*, 277–284. [CrossRef] [PubMed]
58. Chen, J.; Nan, J.; Xu, D.; Mo, L.; Zheng, Y.; Chao, L.; Qu, H.; Guo, Y.; Li, F.; Bao, Y. Response differences between soil fungal and bacterial communities under opencast coal mining disturbance conditions. *Catena* **2020**, *194*, 104779. [CrossRef]
59. Lu, D.; Mao, Z.; Tang, Y.; Feng, B.; Xu, L. Driving Factors Influencing Soil Microbial Community Succession of Coal Mining Subsidence Areas during Natural Recovery in Inner Mongolia Grasslands. *Microorganisms* **2024**, *12*, 87. [CrossRef]
60. Genesio, L.; Miglietta, F.; Lugato, E.; Baronti, S.; Pieri, M.; Vaccari, F.P. Surface albedo following biochar application in durum wheat thermal properties of loess. *Rock Soil Mech.* **2017**, *38*, 2888–2894. [CrossRef]
61. Wang, M.; Sun, M.; Zhao, Y.; Shi, Y.; Sun, S.; Wang, S.; Zhou, Y.; Chen, L. Seasonal changes of soil microbiota and its association with environmental factors in coal mining subsidence area. *AMB Express* **2023**, *13*, 147. [CrossRef] [PubMed]
62. Schuerings, J.; Jentsch, A.; Hammerl, V.; Lenz, K.; Henry, H.A.L.; Malyshev, A.V.; Kreyling, J. Increased winter soil temperature variability enhances nitrogen cycling and soil biotic activity in temperate heathland and grassland mesocosms. *Biogeosciences* **2014**, *11*, 7051–7060. [CrossRef]
63. Yang, S.; Jansen, B.; Absalah, S.; Kalbitz, K.; Castro, F.O.C.; Cammeraat, E.L.H. Soil organic carbon content and mineralization controlled by the composition, origin and molecular diversity of organic matter: A study in tropical alpine grasslands. *Soil Tillage Res.* **2022**, *215*, 105203. [CrossRef]
64. John, L. Let the Soil Work for Us. *BioScience* **1997**, *47*, 321–322.
65. Kravchenko, A.N.; Guber, A.K. Soil pores and their contributions to soil carbon processes. *Geoderma* **2016**, *287*, 31–39. [CrossRef]
66. Juarez, S.; Nunan, N.; Duday, A.C.; Pouteau, V.; Schmidt, S.; Hapca, S.; Falconer, R.; Otten, W.; Chenu, C. Effects of different soil structures on the decomposition of native and added organic carbon. *Eur. J. Soil Biol.* **2013**, *58*, 81–90. [CrossRef]
67. Juarez, S.; Nunan, N.; Duday, A.C.; Pouteau, V.; Chenu, C. Soil carbon mineralisation responses to alterations of microbial diversity and soil structure. *Biol. Fertil. Soils* **2013**, *49*, 939–948. [CrossRef]
68. Gaillard, V.; Chenu, C.; Recous, S. Carbon mineralisation in soil adjacent to plant residues of contrasting biochemical quality. *Soil Biol. Biochem.* **2003**, *35*, 93–99. [CrossRef]
69. Toosi, E.R.; Kravchenko, A.N.; Guber, A.K.; Rivers, M.L. Pore characteristics regulate priming and fate of carbon from plant residue. *Soil Biol. Biochem.* **2017**, *113*, 219–230. [CrossRef]
70. Ruamps, L.S.; Nunan, N.; Chenu, C. Microbial biogeography at the soil pore scale. *Soil Biol. Biochem.* **2011**, *43*, 280–286. [CrossRef]
71. Dechesne, A.; Pallud, C.; Debouzie, D.; Flandrois, J.P.; Vogel, T.M.; Gaudet, J.P.; Grundmann, G.L. A novel method for characterizing the microscale 3D spatial distribution of bacteria in soil. *Soil Biol. Biochem.* **2003**, *35*, 1537–1546. [CrossRef]

72. Kravchenko, A.N.; Negassa, W.; Guber, A.K.; Schmidt, S. New Approach to Measure Soil ParticulateOrganic Matter in Intact Samples Using X-ray Computed Microtomography. *Soil Sci. Soc. Am. J.* **2014**, *78*, 1177–1185. [CrossRef]

73. Negassa, W.C.; Guber, A.K.; Kravchenko, A.N.; Marsh, T.L.; Britton, H.; Rivers, M.L.; Wenju, L. Properties of Soil Pore Space Regulate Pathways of Plant Residue Decomposition and Community Structure of Associated Bacteria. *PLoS ONE* **2015**, *10*, e123999. [CrossRef]

74. Cambi, M.; Certini, G.; Neri, F.; Marchi, E. The impact of heavy traffic on forest soils: A review. *For. Ecol. Manag.* **2015**, *338*, 124–138. [CrossRef]

75. Indorante, S.J.; Jansen, I.J.; Boast, C.W. Surface mining and reclamation: Initial changes in soil character. *J. Soil Water Conserv.* **1981**, *36*, 347–351.

76. Frouz, J. Development of soil microbial properties in topsoil layer during spontaneous succession in heaps after brown coal mining in relation to humus microstructure development. *Geoderma* **2005**, *129*, 54–64. [CrossRef]

77. Feng, Y.; Wang, J.; Bai, Z.; Reading, L. Effects of surface coal mining and land reclamation on soil properties: A review. *Earth-Sci. Rev.* **2019**, *191*, 12–25. [CrossRef]

78. Zipper, C.E.; Burger, J.A.; Skousen, J.G.; Angel, P.N.; Barton, C.D.; Davis, V.; Franklin, J.A. Restoring Forests and Associated Ecosystem Services on Appalachian Coal Surface Mines. *Environ. Manag.* **2011**, *47*, 751–765. [CrossRef]